

1

2 Modular strategies for spatial mapping of 3 multi-modal mouse brain data

4 Nicholas J. Tustison¹, Min Chen², Fae N. Kronman³, Jeffrey T. Duda², Clare Gamlin⁴, Mia
5 G. Tustison, Michael Kunst⁴, Rachel Dalley⁴, Staci Sorenson⁴, Quanxin Wang⁴, Lydia Ng⁴,
6 Yongsoo Kim³, and James C. Gee²

7 ¹Department of Radiology and Medical Imaging, University of Virginia, Charlottesville, VA

8 ²Department of Radiology, University of Pennsylvania, Philadelphia, PA

9 ³Department of Neuroscience and Experimental Therapeutics, Penn State University, Hershey, PA

10 ⁴Allen Institute for Brain Science, Seattle, WA

11

12 Corresponding authors:

13

14 Nicholas J. Tustison, DSc

15 Department of Radiology and Medical Imaging

16 University of Virginia

17 ntustison@virginia.edu

18

19 James C. Gee, PhD

20 Department of Radiology

21 University of Pennsylvania

22 gee@upenn.edu

²³ **Abstract**

²⁴ Large-scale efforts by the BRAIN Initiative Cell Census Network (BICCN) are generating a
²⁵ comprehensive reference atlas of cell types in the mouse brain. A key challenge in this effort
²⁶ is mapping diverse datasets, acquired with varied imaging, tissue processing, and profiling
²⁷ methods, into shared coordinate frameworks. Here, we present modular mapping pipelines
²⁸ developed using the Advanced Normalization Tools Ecosystem (ANTsX) to align MERFISH
²⁹ spatial transcriptomics and high-resolution fMOST morphology data to the Allen Common
³⁰ Coordinate Framework (CCFv3), and developmental MRI and LSFM data to the Devel-
³¹ opmental CCF (DevCCF). Simultaneously, we introduce two novel methods: 1) a velocity
³² field-based approach for continuous interpolation across developmental timepoints, and 2)
³³ a deep learning framework for automated brain parcellation using minimally annotated and
³⁴ publicly available data. All workflows are open-source and reproducible. We also provide
³⁵ general guidance for selecting appropriate strategies across modalities, enabling researchers
³⁶ to adapt these tools to new data.

³⁷ Introduction

³⁸ Over the past decade, there have been significant advancements in mesoscopic single-cell
³⁹ analysis of the mouse brain. It is now possible to track single neurons¹, observe whole-
⁴⁰ brain developmental changes at cellular resolution², associate brain regions with genetic
⁴¹ composition³, and locally characterize neural connectivity⁴. These scientific achievements
⁴² have been propelled by high-resolution profiling and imaging techniques that enable sub-
⁴³ micron, multimodal, 3D characterizations of whole mouse brains. Among these are micro-
⁴⁴ optical sectioning tomography^{5,6}, tissue clearing methods^{1,7}, spatial transcriptomics^{8,9}, and
⁴⁵ single-cell genomic profiling¹⁰, each offering expanded specificity and resolution for cell-level
⁴⁶ brain analysis.

⁴⁷ Recent efforts by the NIH BRAIN Initiative have mobilized large-scale international collabora-
⁴⁸ tions to create a comprehensive reference database of mouse brain structure and function.
⁴⁹ The BRAIN Initiative Cell Census Network has aggregated over 40 multimodal datasets from
⁵⁰ more than 30 research groups¹¹, many of which are registered to standardized anatomical co-
⁵¹ ordinate systems to support integrated analysis. Among the most widely used of these frame-
⁵² works is the Allen Mouse Brain Common Coordinate Framework (CCFv3)¹². Other CCFs
⁵³ include modality-specific references^{13–15} and developmental atlases^{16,17} that track structural
⁵⁴ change across time.

⁵⁵ Mouse brain mapping challenges

⁵⁶ Robust mapping of cell type data into CCFs is essential for integrative analysis of morphology,
⁵⁷ connectivity, and molecular identity. However, each modality poses unique challenges. For
⁵⁸ example, differences in tissue processing, imaging protocols, and anatomical completeness
⁵⁹ often introduce artifacts such as distortion, tearing, holes, and signal dropout^{18–23}. Inten-
⁶⁰ sity differences and partial representations of anatomy can further complicate alignment.
⁶¹ Also, while alternative strategies for mapping single-cell spatial transcriptomic data exist
⁶² (e.g., gene expression-based models such as Tangram²⁴) this work focuses on image-based
⁶³ anatomical alignment to common coordinate frameworks using spatially resolved reference

64 images. Given this diversity specialized strategies are often needed to address the unique,
65 modality-specific challenges.

66 Existing mapping solutions fall into three broad categories. The first includes integrated
67 processing platforms that provide users with mapped datasets (e.g., Allen Brain Cell
68 Atlas²⁵, Brain Architecture Portal²⁶, OpenBrainMap²⁷, and Image and Multi-Morphology
69 Pipeline²⁸). These offer convenience and high-quality curated data, but limited gener-
70 alizability and customization. The second category involves highly specialized pipelines
71 tailored to specific modalities such as histology^{29–31}, magnetic resonance imaging (MRI)^{32–34},
72 microCT^{35,36}, light sheet fluorescence microscopy (LSFM)^{37,38}, flourescence micro-optical
73 sectioning tomography (fMOST)^{15,39}, and spatial transcriptomics, including multiplexed
74 error-robust fluorescence *in situ* hybridization (MERFISH)^{40–42}. While effective, these
75 solutions often require extensive engineering effort to adapt to new datasets or modal-
76 ities. Finally, general-purpose toolkits such as elastix⁴³, Slicer3D⁴⁴, and the Advanced
77 Normalization Tools Ecosystem (ANTsX)⁴⁵ have all been applied to mouse brain mapping
78 scenarios. These toolkits support modular workflows that can be flexibly composed from
79 reusable components, offering a powerful alternative to rigid, modality-specific solutions.
80 However, their use often requires familiarity with pipeline modules, parameter tuning, and
81 tool-specific conventions which can limit adoption.

82 Building on this third category, we describe a set of modular, ANTsX-based pipelines specif-
83 ically tailored for mapping diverse mouse brain data into standardized anatomical frame-
84 works. These include two new pipelines: a velocity field-based interpolation model that
85 enables continuous transformations across developmental timepoints of the DevCCF, and a
86 template-based deep learning pipeline for whole brain segmentation (i.e., brain extraction)
87 and structural anatomical regional labeling of the brain (i.e., brain parcellation) requiring
88 minimal annotated data. In addition, we include two modular pipelines for aligning MER-
89 FISH and fMOST datasets to the Allen CCFv3. These workflows were adapted and tailored
90 using ANTsX tools to support collaborative efforts within the BICCN and are now made
91 openly available in a reproducible format. To facilitate broader adoption, we also provide
92 general guidance for customizing these strategies across imaging modalities and data types.

93 We first introduce key components of the ANTsX toolkit, which provide a basis for all of the
94 mapping workflows described here, and then detail the specific contributions made in each
95 pipeline.

96 **The Advanced Normalization Tools Ecosystem (ANTsX)**

97 The Advanced Normalization Tools Ecosystem (ANTsX) has been used in a number of
98 applications for mapping mouse brain data as part of core processing steps in various
99 workflows^{31,46–49}, particularly its pairwise, intensity-based image registration capabilities⁵⁰
100 and bias field correction⁵¹. Historically, ANTsX development is based on foundational ap-
101 proaches to image mapping^{52–54}, especially in the human brain, with key contributions such
102 as the Symmetric Normalization (SyN) algorithm⁵⁰. It has been independently evaluated
103 in diverse imaging domains including multi-site brain MRI⁵⁵, pulmonary CT⁵⁶, and multi-
104 modal brain tumor registration⁵⁷. More recent contributions for mouse-specific applications
105 showcase multimodal template generation¹⁶ and anatomy-aware registration⁵⁸ ANTsX func-
106 tionality.

107 Beyond registration, ANTsX provides functionality for template generation⁵⁹, segmentation⁶⁰,
108 preprocessing^{51,61}, and deep learning⁴⁵. It has demonstrated strong performance in consen-
109 sus labeling⁶², brain tumor segmentation⁶³, and cardiac motion estimation⁶⁴. Built on the
110 Insight Toolkit (ITK)⁶⁵, ANTsX benefits from open-source contributions while supporting
111 continued algorithm evaluation and innovation. In the context of mouse brain data, ANTsX
112 provides a robust platform for developing modular pipelines to map diverse imaging modal-
113 ities into CCFs. These tools span multiple classes of mapping problems: cross-modality
114 image registration, landmark-driven alignment, temporal interpolation across developmental
115 stages, and deep learning-based segmentation. As such, they also serve as illustrative case
116 studies for adapting ANTsX tools to other use cases. We describe both shared infrastructure
117 and targeted strategies adapted to the specific challenges of each modality. This paper
118 highlights usage across distinct BICCN projects such as spatial transcriptomic data from
119 MERFISH, structural data from fMOST, and multimodal developmental data from LSFM
120 and MRI.

¹²¹ **Novel ANTsX-based open-source contributions**

¹²² We introduce two novel contributions to ANTsX developed as part of collaborative efforts
¹²³ in creating the Developmental Common Coordinate Framework (DevCCF)¹⁶. First, we
¹²⁴ present an open-source velocity field-based interpolation framework for continuous map-
¹²⁵ ping across the sampled embryonic and postnatal stages of the DevCCF atlas¹⁶. This
¹²⁶ functionality enables biologically plausible interpolation between timepoints via a time-
¹²⁷ parameterized diffeomorphic velocity model⁶⁶, inspired by previous work⁶⁷. Second, we
¹²⁸ present a deep learning pipeline for structural parcellation of the mouse brain from mul-
¹²⁹ timodal MRI data. This includes two novel components: 1) a template-derived brain ex-
¹³⁰ traction model using augmented data from two ANTsX-derived template datasets^{68,69}, and
¹³¹ 2) a template-derived parcellation model trained on DevCCF P56 labelings mapped from
¹³² the AllenCCFv3. This pipeline demonstrates how ANTsX tools and public resources can be
¹³³ leveraged to build robust anatomical segmentation pipelines with minimal annotated data.
¹³⁴ We independently evaluate this framework using a longitudinal external dataset⁷⁰, demon-
¹³⁵ strating generalizability across specimens and imaging protocols. All components are openly
¹³⁶ available through the R and Python ANTsX packages, with general-purpose functionality
¹³⁷ documented in a reproducible, cross-platform tutorial (<https://tinyurl.com/antsxtutorial>).
¹³⁸ Code specific to this manuscript, including scripts to reproduce the novel contributions
¹³⁹ and all associated evaluations, is provided in a dedicated repository (<https://github.com/>
¹⁴⁰ [ntustison/ANTsXMouseBrainMapping](https://github.com/ntustison/ANTsXMouseBrainMapping)). Additional tools for mapping spatial transcriptomic
¹⁴¹ (MERFISH) and structural (fMOST) data to the AllenCCFv3 are separately available at
¹⁴² (<https://github.com/dontminchenit/CCFAAlignmentToolkit>).

143 **Results**

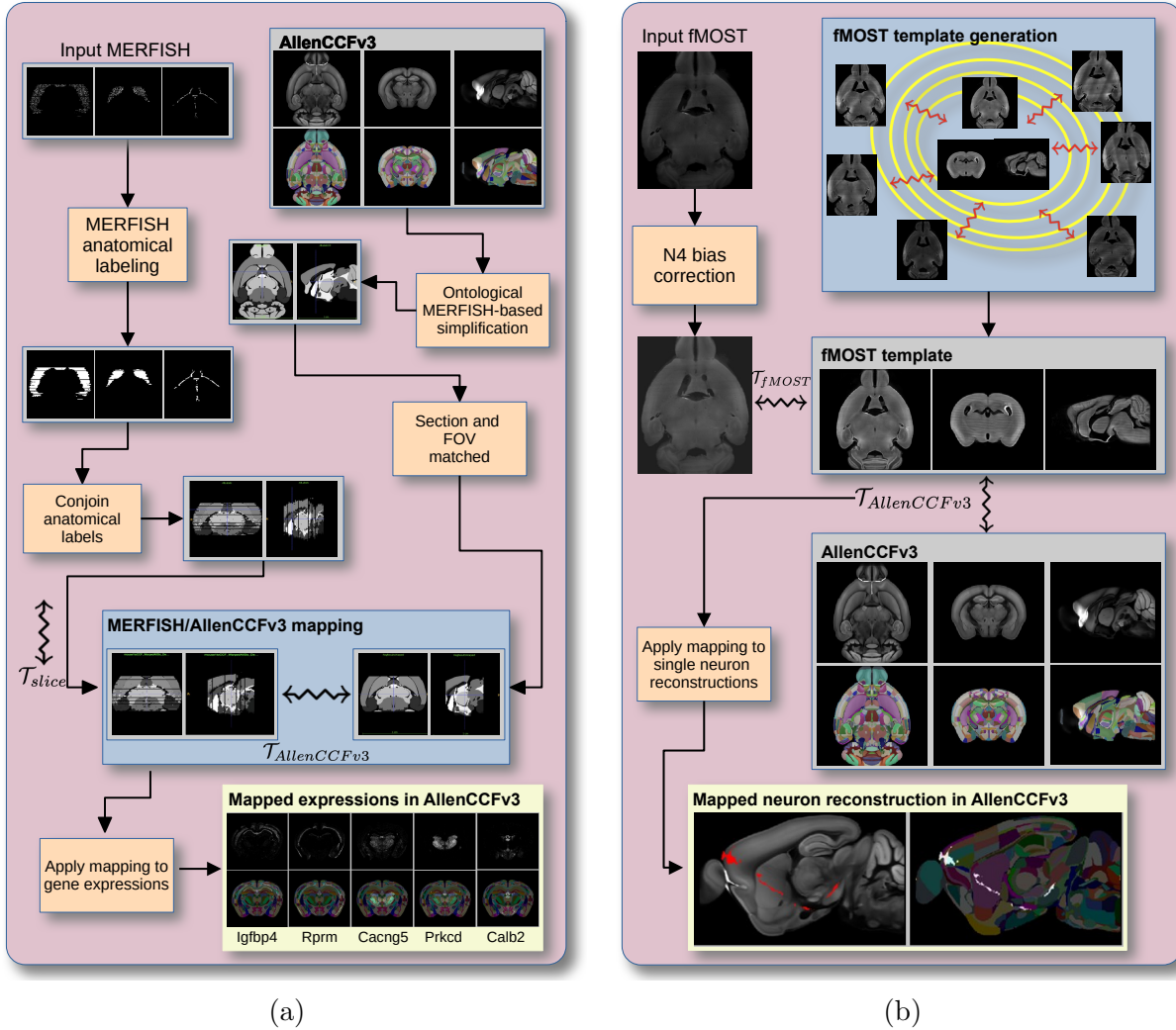


Figure 1: Diagram of the two ANTsX-based pipelines for mapping (a) MERFISH and (b)fMOST data into the space of AllenCCFv3. Each generates the requisite transforms to map individual images to the CCF.

144 **AllenCCFv3 brain image mapping**

145 **Mapping multiplexed error-robust fluorescence *in situ* hybridization (MER-
146 FISH) data**

147 **Overview.** We developed an ANTsX-based pipeline to map spatial transcriptomic MER-
148 FISH data into the AllenCCFv3 (Figure 1(a)). This approach was used in recent efforts to

¹⁴⁹ create a high-resolution transcriptomic atlas of the mouse brain⁴⁹. The pipeline maps spatial gene expression patterns from MERFISH onto anatomical labels in the AllenCCFv3. It includes MERFISH-specific preprocessing steps such as section reconstruction, label generation from spatial transcriptomic maps, and anatomical correspondence mapping. Alignment proceeds in two stages: 1) 3D affine registration and section matching of the AllenCCFv3 to the MERFISH data, and 2) linear + deformable 2D section-wise alignment between matched MERFISH and atlas slices. These transformations are concatenated to produce a complete mapping from each MERFISH data to AllenCCFv3.

¹⁵⁷ **Data.** MERFISH imaging was performed on cryosectioned brains from C57BL/6 mice using previously described protocols⁴⁹. Brains were placed into an optimal cutting temperature (OCT) compound (Sakura FineTek 4583) stored at -80°. The fresh frozen brain was sectioned at 10 μ m on Leica 3050 S cryostats at intervals of 200 μ m to evenly cover the brain. A set of 500 genes was selected to distinguish \sim 5200 transcriptomic clusters. Raw MERSCOPE data were decoded using Vizgen software (v231). Cell segmentation was performed using Cellpose^{71,72} based on DAPI and PolyT stains which was propagated to adjacent slices across z-planes. Each MERFISH cell was assigned a transcriptomic identity by mapping to a scRNA-seq reference taxonomy.

¹⁶⁶ **Evaluation.** Alignment quality was evaluated iteratively by an expert anatomist, guided by expected gene-marker correspondences to AllenCCFv3 regions. As previously reported⁴⁹, further assessment of the alignment showed that, of the 554 terminal regions (gray matter only in the AllenCCFv3), only seven small subregions did not contain cells from the MERFISH dataset post registration: frontal pole, layer 1 (FRP1), FRP2/3, FRP5; accessory olfactory bulb, glomerular layer (AOBgl); accessory olfactory bulb, granular layer (AOBgr); accessory olfactory bulb, mitral layer (AOBmi); and accessory supraoptic group (ASO).

¹⁷³ Mapping fluorescence micro-optical sectioning tomography (fMOST) data

¹⁷⁴ **Overview.** We also constructed a pipeline for mapping fMOST images to the AllenCCFv3 using ANTsX (Figure 1(b)). The approach leverages a modality-specific average fMOST atlas as an intermediate target, adapted from previous work in human and mouse brain

¹⁷⁷ mapping^{12,15,16,59,73–76}. The atlas was constructed from 30 fMOST images selected to cap-
¹⁷⁸ ture representative variability in anatomical shape and image intensity across the population.
¹⁷⁹ Preprocessing includes cubic B-spline downsampling to match the 25 μm isotropic AllenC-
¹⁸⁰ Cfv3 resolution, stripe artifact suppression using a 3D notch filter implemented with SciPy’s
¹⁸¹ frequency-domain filtering tools, and N4 bias field correction⁵¹. A one-time, annotation-
¹⁸² driven alignment registers the fMOST atlas to AllenCCFv3 using landmark-based registra-
¹⁸³ tion of key structures. This canonical mapping is then reused. New fMOST specimens are
¹⁸⁴ first aligned to the fMOST atlas using standard intensity-based registration, and the con-
¹⁸⁵ catenated transforms yield full spatial normalization to the AllenCCFv3. This same mapping
¹⁸⁶ can be applied to neuron reconstructions to facilitate population-level analysis of morphology
¹⁸⁷ and spatial distribution.

¹⁸⁸ **Data.** fMOST imaging was performed on 55 mouse brains with sparse transgenic labeling
¹⁸⁹ of neuron populations^{77,78} using the high-throughput fMOST platform^{79,80}. Voxel resolution
¹⁹⁰ was $0.35 \times 0.35 \times 1.0 \mu\text{m}^3$. Two imaging channels were acquired: GFP-labeled neuron mor-
¹⁹¹ phology (green), and propidium iodide counterstaining for cytoarchitecture (red). Alignment
¹⁹² was performed using the red channel for its greater contrast, though multi-channel mapping
¹⁹³ is also supported.

¹⁹⁴ **Evaluation.** The canonical mapping from the fMOST atlas to AllenCCFv3 was eval-
¹⁹⁵ uated using both quantitative and qualitative approaches. Dice similarity coefficients were
¹⁹⁶ computed between corresponding anatomical labels in the fMOST atlas and AllenCCFv3
¹⁹⁷ following registration. These labels were manually annotated or adapted from existing atlas
¹⁹⁸ segmentations. Representative Dice scores included: whole brain (0.99), caudate putamen
¹⁹⁹ (0.97), fimbria (0.91), posterior choroid plexus (0.93), anterior choroid plexus (0.96), optic
²⁰⁰ chiasm (0.77), and habenular commissure (0.63). In addition to these quantitative assess-
²⁰¹ ments, each registered fMOST specimen was evaluated qualitatively. An expert anatomist
²⁰² reviewed alignment accuracy and confirmed structural correspondence. Neuron reconstruc-
²⁰³ tions from individual brains were also transformed into AllenCCFv3 space, and their trajec-
²⁰⁴ tories were visually inspected to confirm anatomical plausibility and preservation of known
²⁰⁵ projection patterns.

206 Continuously mapping the DevCCF developmental trajectory

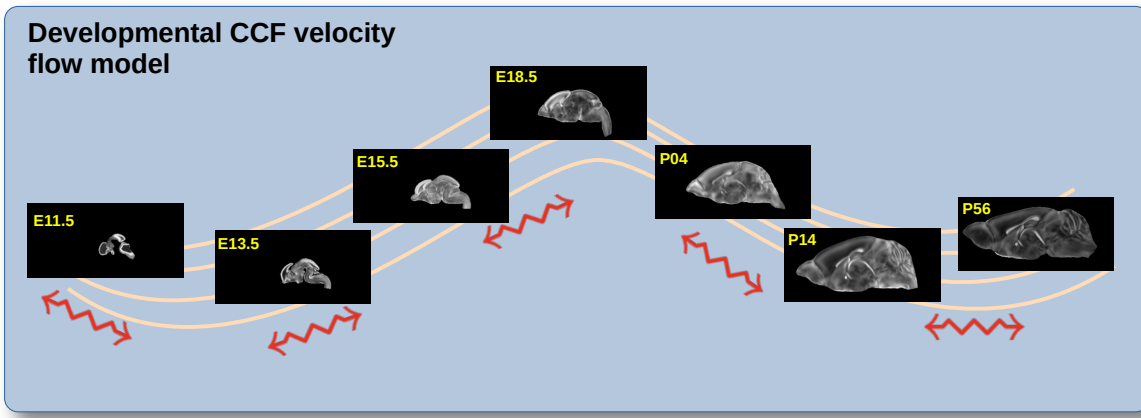


Figure 2: The spatial transformation between any two time points within the continuous DevCCF longitudinal developmental trajectory is available through the use of ANTsX functionality for generating a velocity flow model.

207 The DevCCF is an openly accessible resource for the mouse brain research community¹⁶,
208 comprising symmetric, multi-modal MRI and LSFM templates generated using the ANTsX
209 framework⁵⁹. It spans key stages of mouse brain development (E11.5, E13.5, E15.5, E18.5,
210 P4, P14, and P56) and includes structural labels defined by a developmental ontology.
211 The DevCCF was constructed in coordination with the AllenCCFv3 to facilitate integra-
212 tion across atlases and data types.

213 Although this collection provides broad developmental coverage, its discrete sampling
214 limits the ability to model continuous transformations across time. To address this, we
215 developed a velocity flow-based modeling approach that enables anatomically plausible,
216 diffeomorphic transformations between any two continuous time points within the De-
217 vCCF range. Unlike traditional pairwise interpolation, which requires sequential warping
218 through each intermediate stage, this model, defined by a time-varying velocity field
219 (i.e., a smooth vector field defined over space and time that governs the continuous
220 deformation of an image domain), allows direct computation of deformations between
221 any two time points in the continuum which improves smoothness and enables flexi-
222 ble spatiotemporal alignment. This functionality is implemented in both ANTsR and

223 ANTsPy (see `ants.fit_time_varying_transform_to_point_sets(...)`) and integrates
 224 seamlessly with existing ANTsX workflows. The velocity field is represented as a 4D
 225 ITK image where each voxel stores the x,y,z components of motion at a given time
 226 point. Integration of the time-varying velocity field uses uses 4th order Runge-Kutta
 227 (`ants.integrate_velocity_field(...)`)⁸¹.

228 **Data**

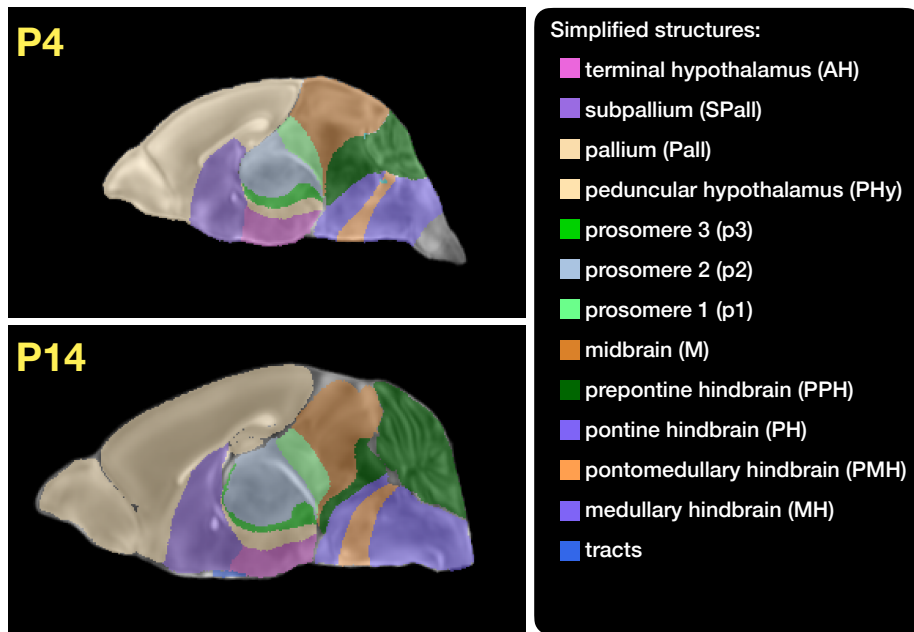


Figure 3: Annotated regions representing common labels across developmental stages, shown for both P4 and P14.

229 Each DevCCF template includes over 2,500 labeled anatomical regions, with spatial reso-
 230 lutions ranging from 31.5 to 50 μm . For the velocity flow modeling task, we identified a
 231 common set of 26 bilateral regions (13 per hemisphere) that were consistently labeled across
 232 all timepoints. These regions span major developmental domains including the pallium, sub-
 233 pallium, midbrain, prosomeres, hypothalamus, hindbrain subregions, and key white matter
 234 tracts (Figure 3).

235 Prior to velocity field optimization, all templates were rigidly aligned to the DevCCF P56
 236 template using the centroids of these common label sets. Pairwise correspondence be-

237 tween adjacent timepoints was then computed using ANTsX’s multi-metric registration via
238 `ants.registration(...)`. Instead of performing intensity-based multi-label registration di-
239 rectly, we constructed 24 binary label masks per atlas pair (one per structure) and optimized
240 alignment using the mean squares similarity metric with the SyN transform⁵⁰.

241 To generate the point sets for velocity field optimization, we sampled both boundary (con-
242 tour) and interior (region) points from the P56 labels and propagated them to each devel-
243 opmental stage using the learned pairwise transforms. Contours were sampled at 10% of
244 available points and regions at 1%, yielding 173,303 total points per atlas ($N_{contour} = 98,151$;
245 $N_{region} = 75,152$). Boundary points were assigned double weight during optimization to
246 emphasize anatomical boundary correspondence.

247 Velocity field optimization

248 The velocity field was optimized using the seven corresponding point sets and their associated
249 weights. The field geometry was defined at [256, 182, 360] with 11 integration points at 50
250 μm resolution, yielding a compressed velocity model of ~ 2 GB. This resolution balanced
251 accuracy and computational tractability while remaining portable. All data and code are
252 publicly available in the accompanying GitHub repository.

253 To normalize temporal spacing, we assigned scalar values in [0, 1] to each template. Given
254 the nonlinear spacing in postnatal development, we applied a logarithmic transform to the
255 raw time values prior to normalization. Within this logarithmic temporal transform, P56
256 was assigned a span of 28 postnatal days to reflect known developmental dynamics (i.e., in
257 terms of modeling the continuous deformation, the morphological changes between Day 28
258 and Day 56 are insignificant). This improved the temporal distribution of integration points
259 (Figure 4, right panel).

260 Optimization was run for a maximum of 200 iterations using a 2020 iMac (3.6 GHz 10-Core
261 Intel Core i9, 64 GB RAM), with each iteration taking ~ 6 minutes. During each iteration,
262 the velocity field was updated across all 11 integration points by computing regularized
263 displacement fields between warped point sets at adjacent time slices. Updates were applied
264 using a step size of $\delta = 0.2$. Convergence was assessed via average displacement error across

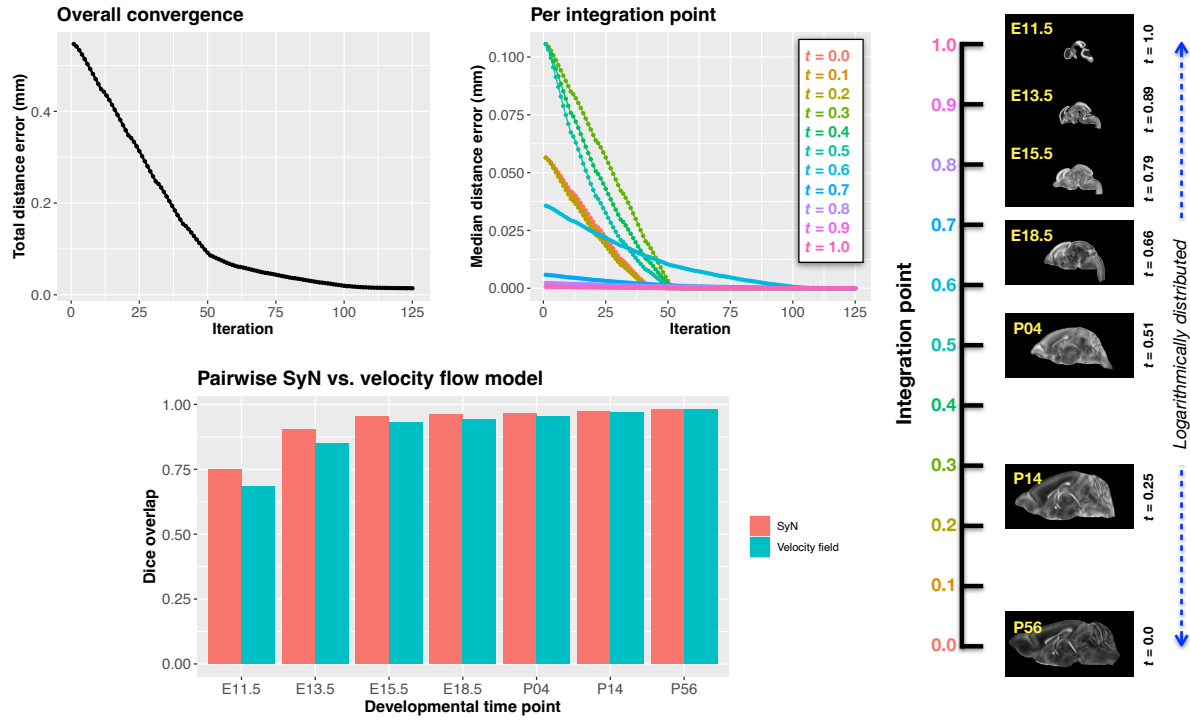


Figure 4: Convergence and evaluation of the velocity flow model across the DevCCF developmental trajectory. (Top left) Total displacement error over iterations. (Top right) Median displacement error per integration point across the optimization timeline, spanning embryonic (E11.5) to postnatal (P56) stages. (Bottom) Dice similarity scores comparing region-level label overlap between: (1) conventional pairwise SyN registration and (2) velocity flow-based deformation, across intermediate timepoints. Using region-based pairwise registration with SyN as a performance upper bound, the velocity flow model achieves comparable accuracy while also enabling smooth, continuous deformation across the full developmental continuum.

265 all points, with final convergence achieved after ~ 125 iterations (Figure 4, left panel).
 266 Median errors across integration points also trended toward zero, albeit at varying rates.
 267 To benchmark performance, we compared the velocity model’s region-based alignment to
 268 traditional pairwise registration using SyN, a widely used diffeomorphic algorithm. The
 269 velocity model achieved comparable Dice scores at sampled timepoints while additionally
 270 offering smooth interpolation across the entire developmental trajectory.

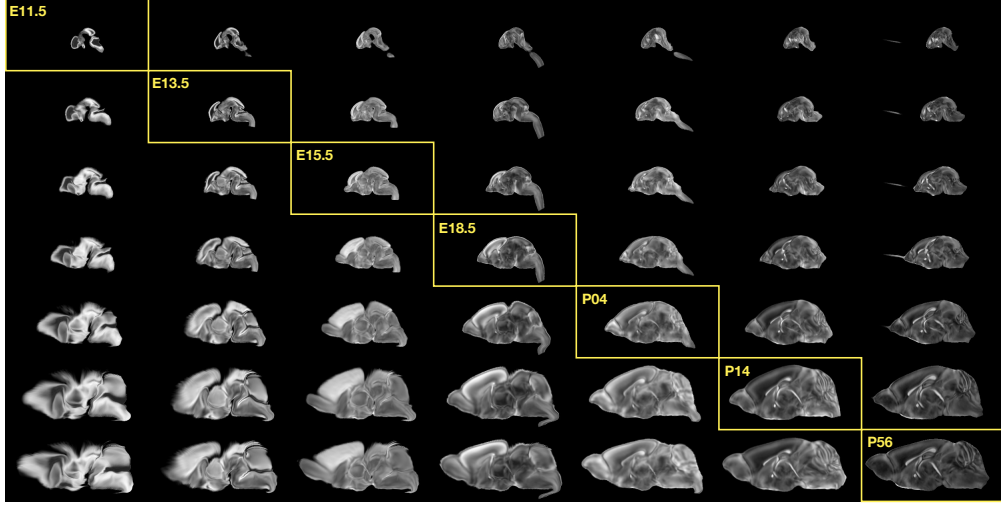


Figure 5: Mid-sagittal visualization of DevCCF templates warped to every other time point. Each row is a reference space; each column is a warped input. Diagonal entries show original templates.

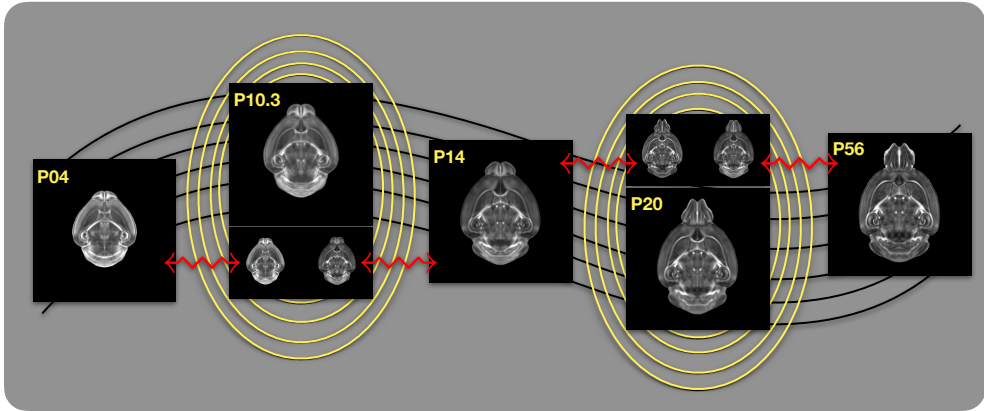


Figure 6: Example of generating “virtual” DevCCF templates at intermediate time points (e.g., P10.3, P20) by warping adjacent stages to a shared time and averaging using ANTsX.

271 The velocity flow transformation model

272 Once optimized, the velocity field enables the computation of diffeomorphic transformations
 273 between any pair of continuous time points within the DevCCF developmental range. Fig-
 274 ure 5 illustrates cross-warping between all DevCCF stages using the velocity flow model. In
 275 addition to facilitating flexible alignment between existing templates, the model also sup-
 276 ports the synthesis of virtual templates at intermediate, unsampled developmental stages.
 277 As shown in Figure 6, we demonstrate the creation of virtual age templates (e.g., P10.3 and

278 P20) by warping adjacent developmental atlases to a target timepoint and constructing an
279 averaged representation using ANTsX’s template-building functionality.

280 All usage examples, scripts, and supporting data for full reproducibility are publicly available
281 in the associated codebase.

282 **Automated structural labeling of the mouse brain**

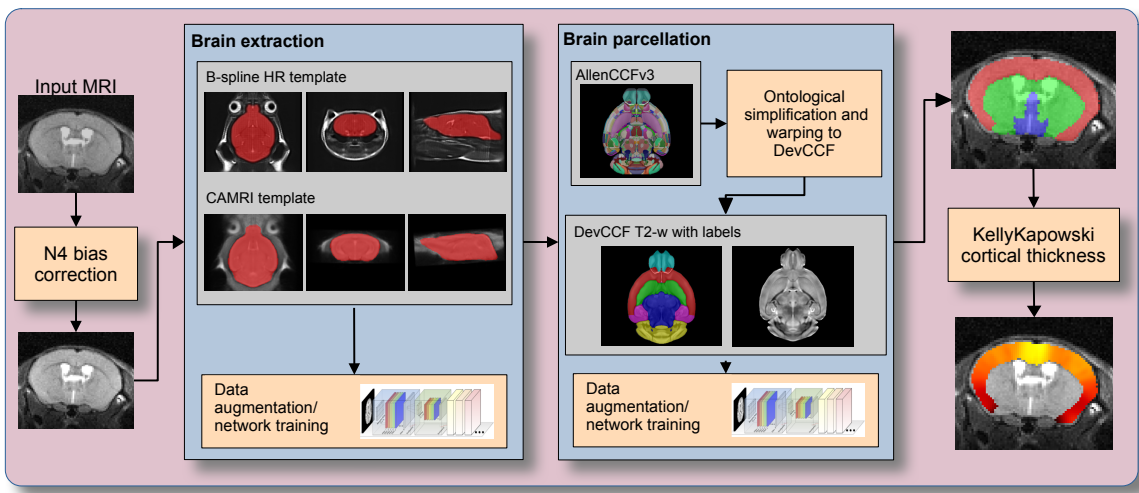


Figure 7: The mouse brain cortical labeling pipeline integrates two deep learning components for brain extraction and anatomical region segmentation. Both networks rely heavily on data augmentation applied to templates constructed from open datasets. The framework also supports further refinement or alternative label sets tailored to specific research needs. Possible applications include voxelwise cortical thickness estimation.

283 Structural labeling strategies for the mouse brain are essential for understanding the organiza-
284 tion and function of the murine nervous system⁸². By dividing the brain into anatomically
285 or functionally defined regions, researchers can localize biological processes, relate regional
286 features to behavior, or quantify spatial variation in gene expression patterns^{83,84}. While
287 deep learning techniques have yielded robust segmentation and labeling tools for the hu-
288 man brain (e.g., SynthSeg⁸⁵, ANTsXNet⁴⁵), analogous development for mouse data (e.g.,
289 MEMOS⁸⁶) has been limited. Mouse neuroimaging often presents unique challenges, such
290 as highly anisotropic sampling, that complicate transfer of existing tools. At the same time,
291 high resolution resources like the AllenCCFv3 and DevCCF provide reference label sets that

292 can serve as training data. We demonstrate how ANTsX can be used to construct a full
293 structural labeling pipeline for the mouse brain (Figure 7), including both whole brain seg-
294 mentation (i.e., brain extraction) and the subsequent template-based region segmentation.

295 **Template-based mouse brain extraction network**

296 To develop a general-purpose mouse brain extraction model, we constructed whole-head
297 templates from two publicly available T2-weighted datasets. The first dataset, from the
298 Center for Animal MRI (CAMRI) at the University of North Carolina at Chapel Hill⁶⁸,
299 includes 16 isotropic MRI volumes acquired at $0.16 \times 0.16 \times 0.16$ mm³ resolution. The second
300 dataset⁶⁹ comprises 88 specimens acquired in three orthogonal 2D views (coronal, axial,
301 sagittal) at 0.08×0.08 mm³ in-plane resolution with 0.5 mm slice thickness. These orthogonal
302 2D acquisitions were reconstructed into high-resolution 3D volumes using a B-spline fitting
303 algorithm⁸⁷. Using this synthesized dataset and the CAMRI images, we created two ANTsX-
304 based population templates⁵⁹, each paired with a manually delineated brain mask. These
305 served as the basis for training an initial template-based brain extraction model. Deep
306 learning training of the network employed aggressive data augmentation strategies, including
307 bias field simulation, histogram warping, random spatial deformation, noise injection, and
308 anisotropic resampling. This enabled the model to generalize beyond the two templates.
309 The initial model was released through ANTsXNet and made publicly available.

310 Subsequent community use led to further improvements. A research group applying the
311 tool to their own ex vivo T2-weighted mouse brain data contributed a third template and
312 associated mask (acquired at 0.08 mm isotropic resolution). Incorporating this into the
313 training data improved robustness and accuracy to an independent dataset and extended
314 the model's generalizability. The refined model is distributed through ANTsPyNet via
315 `antspynet.mouse_brain_extraction(...)`.

316 **Template-based mouse brain anatomical labeling**

317 The AllenCCFv3 atlas and its hierarchical ontology, along with the DevCCF, provide a strong
318 foundation for developing region-wise anatomical labeling models for multi-modal mouse

319 brain imaging. Using the `allensdk` Python library, we generated a coarse segmentation
 320 scheme by grouping anatomical labels into six major regions: cerebral cortex, cerebral nuclei,
 321 brainstem, cerebellum, main olfactory bulb, and hippocampal formation. These labels were
 322 mapped onto the P56 T2-weighted DevCCF template to serve as training targets. We trained
 323 a 3D U-net-based segmentation network using this template and the same augmentation
 324 strategies described for brain extraction. The model is publicly available via ANTsXNet
 325 (`antspynet.mouse_brain_parcellation(...)`) and supports robust anatomical labeling
 326 across diverse imaging geometries and contrasts. The inclusion of aggressive augmentation,
 327 including simulated anisotropy, enables the model to perform well even on thick-slice input
 328 data. Internally, the model reconstructs isotropic probability and label maps, facilitating
 329 downstream morphometric analyses. For example, this network integrates with the ANTsX
 330 cortical thickness estimation pipeline (`antspynet.mouse_cortical_thickness(...)`) to
 331 produce voxelwise cortical thickness maps, even when applied to anisotropic or limited-
 332 resolution mouse brain data.

333 **Evaluation**

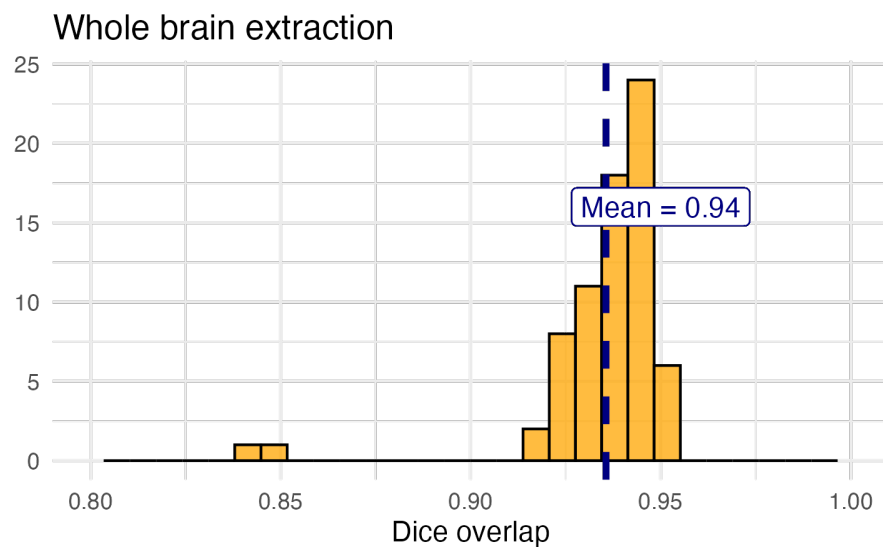
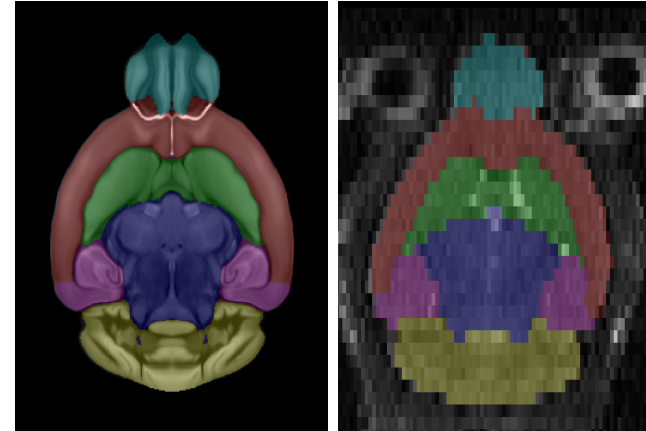
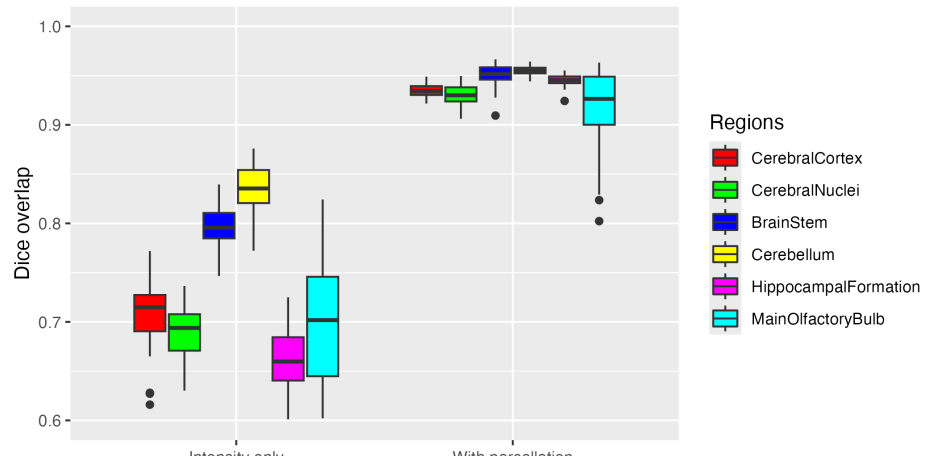


Figure 8: Evaluation of the ANTsX mouse brain extraction on an independent, publicly available dataset consisting of 12 specimens \times 7 time points = 84 total images. Dice overlap comparisons with the user-generated brain masks provide good agreement with the automated results from the brain extraction network.



(a)
Normalization to AllenCCFv3

(b)



(c)

Figure 9: Evaluation of the ANTsX deep learning-based mouse brain parcellation on a diverse MRI cohort. (a) T2-weighted DevCCF P56 template with the six-region parcellation: cerebral cortex, nuclei, brain stem, cerebellum, main olfactory bulb, and hippocampal formation. (b) Example segmentation result from a representative subject (NR5, Day 0) using the proposed deep learning pipeline. (c) Dice overlap scores across the full evaluation cohort ($n = 84$), comparing anatomical alignment achieved via registration using intensity alone versus registration guided by the predicted parcellation. Dice values were computed using manually segmented labels transformed to AllenCCFv3 space.

³³⁴ For evaluation, we used an additional publicly available dataset⁷⁰ that is completely inde-
³³⁵ pendent from the data used in training the brain extraction and parcellation networks. Data
³³⁶ includes 12 specimens each imaged at seven time points (Day 0, Day 3, Week 1, Week 4,
³³⁷ Week 8, Week 20) with in-house-generated brain masks (i.e., produced by the data providers)
³³⁸ for a total of 84 images. Spacing is anisotropic with an in-plane resolution of $0.1 \times 0.1 \text{ mm}^2$
³³⁹ and a slice thickness of 0.5 mm.

³⁴⁰ Figure 8 summarizes the whole-brain overlap between manually segmented reference masks
³⁴¹ and the predicted segmentations for all 84 images in the evaluation cohort. The proposed
³⁴² network demonstrates excellent performance in brain extraction across a wide age range. To
³⁴³ further assess the utility of the parcellation network, we used the predicted labels to guide
³⁴⁴ anatomically informed registration to the AllenCCFv3 atlas using ANTsX multi-component
³⁴⁵ registration, and compared this to intensity-only registration (Figure 9). While intensity-
³⁴⁶ based alignment performs reasonably well, incorporating the predicted parcellation signifi-
³⁴⁷cantly improves regional correspondence. Dice scores shown in Figure 9(c) were computed
³⁴⁸ using manually segmented labels transformed to AllenCCFv3 space.

349 **Discussion**

350 The diverse mouse brain cell type profiles gathered through BICCN and associated efforts
351 provide a rich multi-modal resource to the research community. However, despite significant
352 progress, optimal leveraging of these valuable resources remains an ongoing challenge. A
353 central component to data integration is accurately mapping novel cell type data into com-
354 mon coordinate frameworks (CCFs) for subsequent processing and analysis. To meet these
355 needs, tools for mapping mouse brain data must be both broadly accessible and capable of
356 addressing challenges unique to each modality. In this work, we described modular ANTsX-
357 based pipelines developed to support three distinct BICCN efforts encompassing spatial
358 transcriptomic, morphological, and developmental data. We demonstrated how a flexible
359 image analysis toolkit like ANTsX can be tailored to address specific modality-driven con-
360 straints by leveraging reusable, validated components.

361 The MERFISH mapping pipeline illustrates how ANTsX tools can be adapted to accom-
362 modate high-resolution spatial transcriptomic data. While the general mapping strategy is
363 applicable to other sectioned histological data, the pipeline includes specific adjustments for
364 known anatomical and imaging artifacts present in MERFISH datasets. As such, this exam-
365 ple demonstrates how general-purpose tools can be customized to meet the requirements of
366 highly specialized data types.

367 The fMOST mapping pipeline was developed with the intention of broader applicability.
368 Built primarily from existing ANTsX preprocessing and registration modules, this pipeline
369 introduces an fMOST-specific intermediate atlas to facilitate consistent mappings to the
370 AllenCCFv3. The use of a canonical fMOST atlas reduces the need for repeated manual
371 alignment across new datasets, and the resulting transformations can be directly applied to
372 associated single-neuron reconstructions. This supports integrative morphological analysis
373 across specimens using a common coordinate system.

374 For developmental data, we introduced a velocity field-based model for continuous interpo-
375 lation between discrete DevCCF timepoints. Although the DevCCF substantially expands
376 coverage of developmental stages relative to prior atlases, temporal gaps remain. The ve-

377 locity model enables spatio-temporal transformations within the full developmental interval
378 and supports the generation of virtual templates at unsampled ages. This functionality is
379 built using ANTsX components for velocity field optimization and integration, and offers
380 a novel mechanism for interpolating across the non-linear developmental trajectory of the
381 mouse brain. Such interpolation has potential utility for both anatomical harmonization and
382 longitudinal analyses. Interestingly, long-range transformations (e.g., P56 to E11.5) revealed
383 anatomy evolving in plausible ways yet sometimes diverging from known developmental pat-
384 terns (e.g., hippocampal shape changes) reflecting the input data and offering insight into
385 temporal gaps. These behaviors could assist future efforts to determine which additional
386 time points would most improve spatiotemporal coverage.

387 We also introduced a template-based deep learning pipeline for mouse brain extraction and
388 parcellation using aggressive data augmentation. This approach is designed to reduce the
389 reliance on large annotated training datasets, which remain limited in the mouse imaging
390 domain. Evaluation on independent data demonstrates promising generalization, though
391 further refinement will be necessary. As with our human-based ANTsX pipelines, failure
392 cases can be manually corrected and recycled into future training cycles. Community con-
393 tributions are welcomed and encouraged, providing a pathway for continuous improvement
394 and adaptation to new datasets.

395 The ANTsX ecosystem offers a powerful foundation for constructing scalable, reproducible
396 pipelines for mouse brain data analysis. Its modular design and multi-platform support
397 enable researchers to develop customized workflows without extensive new software devel-
398 opment. The widespread use of ANTsX components across the neuroimaging community
399 attests to its utility and reliability. As a continuation of the BICCN program, ANTsX is
400 well positioned to support the goals of the BRAIN Initiative Cell Atlas Network (BICAN)
401 and future efforts to extend these mapping strategies to the human brain.

402 **Methods**

403 The following methods are all available as part of the ANTsX ecosystem with analogous
404 elements existing in both ANTsR (ANTs in R) and ANTsPy (ANTs in Python), under-
405 pinned by a shared ANTs/ITK C++ core. Most development for the work described was
406 performed using ANTsPy. For equivalent functionality in ANTsR, we refer the reader to the
407 comprehensive ANTsX tutorial: <https://tinyurl.com/antsxtutorial>.

408 **General ANTsX utilities**

409 Although focused on distinct data types, the three pipelines presented in this work share
410 common components that address general challenges in mapping mouse brain data. These
411 include correcting image intensity artifacts, denoising, spatial registration, template gen-
412 eration, and visualization. Table 1 provides a concise summary of the relevant ANTsX
413 functionality.

414 **Preprocessing: bias field correction and denoising.** Standard preprocessing steps in
415 mouse brain imaging include correcting for spatial intensity inhomogeneities and reducing im-
416 age noise, both of which can impact registration accuracy and downstream analysis. ANTsX
417 provides implementations of widely used methods for these tasks. The N4 bias field correction
418 algorithm⁵¹, originally developed in ANTs and contributed to ITK, mitigates artifactual, low-
419 frequency intensity variation and is accessible via `ants.n4_bias_field_correction(...)`.
420 Patch-based denoising⁶¹ has been implemented as `ants.denoise_image(...)`.

421 **Image registration.** ANTsX includes a robust and flexible framework for pairwise
422 and groupwise image registration⁸¹. At its core is the SyN algorithm⁵⁰, a symmetric
423 diffeomorphic model with optional B-spline regularization⁶⁷. In ANTsPy, registration
424 is performed via `ants.registration(...)` using preconfigured parameter sets (e.g.,
425 `antsRegistrationSyNQuick[s]`, `antsRegistrationSyN[s]`) suitable for different imaging
426 modalities and levels of computational demand. Resulting transformations can be applied
427 to new images with `ants.apply_transforms(...)`.

Table 1: Sampling of ANTsX functionality

<i>ANTsPy: Preprocessing</i>	
bias field correction	<code>n4_bias_field_correction(...)</code>
image denoising	<code>denoise_image(...)</code>
<i>ANTsPy: Registration</i>	
intensity image registration	<code>registration(...)</code>
label image registration	<code>label_image_registration(...)</code>
image transformation	<code>apply_transforms(...)</code>
template generation	<code>build_template(...)</code>
landmark registration	<code>fit_transform_to_paired_points(...)</code>
time-varying landmark reg.	<code>fit_time_varying_transform_to_point_sets(...)</code>
integrate velocity field	<code>integrate_velocity_field(...)</code>
invert displacement field	<code>invert_displacement_field(...)</code>
<i>ANTsPy: Segmentation</i>	
MRF-based segmentation	<code>atropos(...)</code>
Joint label fusion	<code>joint_label_fusion(...)</code>
diffeomorphic thickness	<code>kelly_kapowski(...)</code>
<i>ANTsPy: Miscellaneous</i>	
Regional intensity statistics	<code>label_stats(...)</code>
Regional shape measures	<code>label_geometry_measures(...)</code>
B-spline approximation	<code>fit_bspline_object_to_scattered_data(...)</code>
Visualize images and overlays	<code>plot(...)</code>
<i>ANTsPyNet: Mouse-specific</i>	
brain extraction	<code>mouse_brain_extraction(...modality="t2"...)</code>
brain parcellation	<code>mouse_brain_parcellation(...)</code>
cortical thickness	<code>mouse_cortical_thickness(...)</code>
super resolution	<code>mouse_histology_super_resolution(...)</code>

ANTsX provides state-of-the-art functionality for processing biomedical image data. Such tools, including deep learning networks, support a variety of mapping-related tasks. A more comprehensive listing of ANTsX tools with self-contained R and Python examples is provided as a gist page on GitHub (<https://tinyurl.com/antsxtutorial>).

428 **Template generation.** ANTsX supports population-based template generation through it-
429 erative pairwise registration to an evolving estimate of the mean shape and intensity reference
430 space across subjects⁵⁹. This functionality was used in generating the DevCCF templates¹⁶.
431 The procedure, implemented as `ants.build_template(...)`, produces average images in
432 both shape and intensity by aligning all inputs to a common evolving template.

433 **Visualization.** To support visual inspection and quality control, ANTsPy provides flexible
434 image visualization with `ants.plot(...)`. This function enables multi-slice and multi-
435 orientation rendering with optional overlays and label maps.

436 Mapping fMOST data to AllenCCFv3

437 **Preprocessing.** Mapping fMOST data into the AllenCCFv3 presents unique challenges due
438 to its native ultra-high resolution and imaging artifacts common to the fMOST modality.
439 Each fMOST image can exceed a terabyte in size, with spatial resolutions far exceeding
440 those of the AllenCCFv3 ($25\text{ }\mu\text{m}$ isotropic). To reduce computational burden and prevent
441 resolution mismatch, each fMOST image is downsampled using cubic B-spline interpolation
442 via `ants.resample_image(...)` to match the template resolution.

443 Stripe artifacts (i.e., periodic intensity distortions caused by nonuniform sectioning or il-
444 lumination) are common in fMOST and can mislead deformable registration algorithms.
445 These were removed using a custom 3D notch filter (`remove_stripe_artifact(...)`) im-
446 plemented in the `CCFAlignmentToolkit` using SciPy frequency domain filtering. The filter
447 targets dominant stripe frequencies along a user-specified axis in the Fourier domain. In
448 addition, intensity inhomogeneity across sections, often arising from variable staining or
449 illumination, was corrected using N4 bias field correction.

450 **Template-based spatial normalization.** To facilitate reproducible mapping, we first
451 constructed a contralaterally symmetric average template from 30 fMOST brains and their
452 mirrored counterparts using ANTsX template-building tools. Because the AllenCCFv3 and
453 fMOST data differ substantially in both intensity contrast and morphology, direct deformable
454 registration between individual fMOST brains and the AllenCCFv3 was insufficiently robust.

455 Instead, we performed a one-time expert-guided label-driven registration between the aver-
456 age fMOST template and AllenCCFv3. This involved sequential alignment of seven manually
457 selected anatomical regions: 1) brain mask/ventricles, 2) caudate/putamen, 3) fimbria, 4)
458 posterior choroid plexus, 5) optic chiasm, 6) anterior choroid plexus, and 7) habenular
459 commissure which were prioritized to enable coarse-to-fine correction of shape differences.
460 Once established, this fMOST-template-to-AllenCCFv3 transform was reused for all subse-
461 quent specimens. Each new fMOST brain was then registered to the average fMOST tem-
462 plate using intensity-based registration, followed by concatenation of transforms to produce
463 the final mapping into AllenCCFv3 space.

464 **Mapping neuron projections.** A key advantage of fMOST imaging is its ability to support
465 single neuron projection reconstruction across the entire brain⁷⁸. Because these reconstruc-
466 tions are stored as 3D point sets aligned to the original fMOST volume, we applied the same
467 composite transform used for image alignment to the point data using ANTsX functional-
468 ity. This enables seamless integration of cellular morphology data into AllenCCFv3 space,
469 facilitating comparative analyses across specimens.

470 Mapping MERFISH data to AllenCCFv3

471 **Preprocessing.** MERFISH data are acquired as a series of 2D tissue sections, each com-
472 prising spatially localized gene expression measurements at subcellular resolution. To enable
473 3D mapping to the AllenCCFv3, we first constructed anatomical reference images by aggre-
474 gating the number of detected transcripts per voxel across all probes within each section.
475 These 2D projections were resampled to a resolution of $10 \mu m \times 10 \mu m$ to match the in-plane
476 resolution of the AllenCCFv3.

477 Sections were coarsely aligned using manually annotated dorsal and ventral midline points,
478 allowing initial volumetric reconstruction. However, anatomical fidelity remained limited by
479 variation in section orientation, spacing, and tissue loss. To further constrain alignment and
480 enable deformable registration, we derived region-level anatomical labels directly from the
481 gene expression data.

482 **Label creation.** To assign region labels to the MERFISH data, we use a cell type cluster-
483 ing approach previously detailed⁴⁹. In short, manually dissected scRNAseq data was used
484 to establish the distribution of cell types present in each of the following major regions:
485 cerebellum, CTXsp, hindbrain, HPF, hypothalamus, isocortex, LSX, midbrain, OLF, PAL,
486 sAMY, STRd, STRv, thalamus and hindbrain. Clusters in the scRNA-seq dataset were then
487 used to assign similar clusters of cell types in the MERFISH data to the regions they are
488 predominantly found in the scRNA-seq data. To account for clusters that were found at
489 low frequency in regions outside its main region we calculated for each cell its 50 nearest
490 neighbors in physical space and reassigned each cell to the region annotation dominating its
491 neighborhood.

492 **Section matching via global alignment.** A major challenge was compensating for oblique
493 cutting angles and non-uniform section thickness, which distort the anatomical shape and
494 spacing of the reconstructed volume. Rather than directly warping the MERFISH data
495 into atlas space, we globally aligned the AllenCCFv3 to the MERFISH coordinate system.
496 This was done via an affine transformation followed by resampling of AllenCCFv3 sections
497 to match the number and orientation of MERFISH sections. This approach minimizes
498 interpolation artifacts in the MERFISH data and facilitates one-to-one section matching.

499 **Landmark-driven deformable alignment.** We used a 2.5D approach for fine alignment of
500 individual sections. In each MERFISH slice, deformable registration was driven by sequential
501 alignment of anatomical landmarks between the label maps derived from MERFISH and
502 AllenCCFv3. A total of nine regions—including isocortical layers 2/3, 5, and 6, the striatum,
503 hippocampus, thalamus, and medial/lateral habenula—were registered in an empirically
504 determined order. After each round, anatomical alignment was visually assessed by an
505 expert, and the next structure was selected to maximize improvement in the remaining
506 misaligned regions.

507 The final transform for each section combined the global affine alignment and the per-
508 structure deformable registrations. These were concatenated to generate a 3D mapping from
509 the original MERFISH space to the AllenCCFv3 coordinate system. Once established, the
510 composite mapping enables direct transfer of gene-level and cell-type data from MERFISH

511 into atlas space, allowing integration with other imaging and annotation datasets.

512 DevCCF velocity flow transformation model

513 The Developmental Common Coordinate Framework (DevCCF)¹⁶ provides a discrete set of
514 age-specific templates that temporally sample the developmental trajectory. To model this
515 biological progression more continuously, we introduce a velocity flow-based paradigm for in-
516 ferring diffeomorphic transformations between developmental stages. This enables anatomi-
517 cally plausible estimation of intermediate templates or mappings at arbitrary timepoints
518 between the E11.5 and P56 endpoints of the DevCCF. Our approach builds on established
519 insights from time-varying diffeomorphic registration⁶⁶, where a velocity field governs the
520 smooth deformation of anatomical structures over time. Importantly, the framework is ex-
521 tensible and can naturally accommodate additional timepoints for the potential expansion
522 of the DevCCF.

523 **Point sampling and region correspondence.** We first coalesced the anatomical labels
524 across the seven DevCCF templates (E11.5, E13.5, E15.5, E18.5, P4, P14, P56) into 26
525 common structures that could be consistently identified across development. These include
526 major brain regions such as the cortex, cerebellum, hippocampus, midbrain, and ventricles.
527 For each successive pair of templates, we performed multi-label deformable registration us-
528 ing ANTsX to generate forward and inverse transforms between anatomical label volumes.
529 From the P56 space, we randomly sampled approximately 1e6 points within and along the
530 boundaries of each labeled region and propagated them through each pairwise mapping step
531 (e.g., P56 → P14, P14 → P4, . . . , E13.5 → E11.5). This procedure created time-indexed
532 point sets tracing the spatial evolution of each region.

533 **Velocity field fitting.** Using these point sets, we fit a continuous velocity field over develop-
534 mental time using a generalized B-spline scattered data approximation method⁸⁷. The field
535 was parameterized over a log-scaled time axis to ensure finer temporal resolution during early
536 embryonic stages, where morphological changes are most rapid. Optimization proceeded for
537 approximately 125 iterations, minimizing the average Euclidean norm between transformed
538 points at each step. Ten integration points were used to ensure numerical stability. The

539 result is a smooth, differentiable vector field that defines a diffeomorphic transform between
540 any two timepoints within the template range.

541 **Applications and availability.** This velocity model can be used to estimate spa-
542 tial transformations between any pair of developmental stages—even those for which
543 no empirical template exists—allowing researchers to create interpolated atlases, align
544 new datasets, or measure continuous structural changes. It also enables developmental
545 alignment of multi-modal data (e.g., MRI to LSFM) by acting as a unifying spatiotem-
546 poral scaffold. The underlying components for velocity field fitting and integration
547 are implemented in ITK, and the complete workflow is accessible in both ANTsPy
548 (`ants.fit_time_varying_transform_to_point_sets(...)`) and ANTsR. In addition
549 the availability of the DevCCF use case, self-contained examples and usage tutorials are
550 provided in our public codebase.

551 **Automated brain extraction and parcellation with ANTsXNet**

552 To support template-based deep learning approaches for structural brain extraction and par-
553 cellation, we implemented dedicated pipelines using the ANTsXNet framework. ANTsXNet
554 comprises open-source deep learning libraries in both Python (ANTsPyNet) and R (ANTsR-
555 Net) that interface with the broader ANTsX ecosystem and are built on TensorFlow/Keras.
556 Our mouse brain pipelines mirror existing ANTsXNet tools for human imaging but are
557 adapted for species-specific anatomical variation, lower SNR, and heterogeneous acquisition
558 protocols.

559 **Deep learning training setup**

560 All network-based approaches were implemented using a standard U-net⁸⁸ architecture and
561 hyperparameters previously evaluated in ANTsXNet pipelines for human brain imaging⁴⁵.
562 This design follows the ‘no-new-net’ principle⁸⁹, which demonstrates that a well-configured,
563 conventional U-net can achieve robust and competitive performance across a wide range of
564 biomedical segmentation tasks with little to no architectural modifications from the original.

565 Both networks use a 3D U-net architecture implemented in TensorFlow/Keras, with five
566 encoding/decoding levels and skip connections. The loss function combined Dice and cate-
567 gorical cross-entropy terms. Training used a batch size of 4, Adam optimizer with an initial
568 learning rate of 2e-4, and early stopping based on validation loss. Training was performed on
569 an NVIDIA DGX system ($4 \times$ Tesla V100 GPUs, 256 GB RAM). Model weights and prepro-
570 cessing routines are shared across ANTsPyNet and ANTsRNet to ensure reproducibility and
571 language portability. For both published and unpublished trained networks available through
572 ANTsXNet, all training scripts and data augmentation generators are publicly available at
573 <https://github.com/ntustison/ANTsXNetTraining>.

574 **Data augmentation.** Robust data augmentation was critical to generalization across scan-
575 ners, contrast types, and resolutions. We applied both intensity- and shape-based augmen-
576 tation strategies:

577 • *Intensity augmentations:*

- 578 – Gaussian, Poisson, and salt-and-pepper noise:
579 `ants.add_noise_to_image(...)`
- 580 – Simulated intensity inhomogeneity via bias field modeling⁵¹:
581 `antspynet.simulate_bias_field(...)`
- 582 – Histogram warping to simulate contrast variation⁹⁰:
583 `antspynet.histogram_warp_image_intensities(...)`

584 • *Shape augmentations:*

- 585 – Random nonlinear deformations and affine transforms:
586 `antspynet.randomly_transform_image_data(...)`
- 587 – Anisotropic resampling across axial, sagittal, and coronal planes:
588 `ants.resample_image(...)`

589 **Brain extraction**

590 We originally trained a mouse-specific brain extraction model on two manually masked
591 T2-weighted templates, generated from public datasets^{68,69}. One of the templates was
592 constructed from orthogonal 2D acquisitions using B-spline-based volumetric synthesis via
593 `ants.fit_bspline_object_to_scattered_data(...)`. Normalized gradient magnitude
594 was used as a weighting function to emphasize boundaries during reconstruction⁸⁷.

595 This training strategy provides strong spatial priors despite limited data by leveraging high-
596 quality template images and aggressive augmentation to mimic population variability. Dur-
597 ing the development of this work, the network was further refined through community en-
598 gagement. A user from a U.S.-based research institute applied this publicly available (but
599 then unpublished) brain extraction tool to their own mouse MRI dataset. Based on feedback
600 and iterative collaboration with the ANTsX team, the model was retrained and improved to
601 better generalize to additional imaging contexts. This reflects our broader commitment to
602 community-driven development and responsiveness to user needs across diverse mouse brain
603 imaging scenarios.

604 The final trained network is available via ANTsXNet through the function
605 `antspynet.mouse_extraction(...)`. Additionally, both template/mask pairs are
606 accessible via ANTsXNet. For example, one such image pair is available via:

- Template:

```
608     antspynet.get_antsxnet_data("bsplineT2MouseTemplate")
```

- Brain mask:

```
610     antspynet.get_antsxnet_data("bsplineT2MouseTemplateBrainMask")
```

611 **Brain parcellation**

612 For brain parcellation, we trained a 3D U-net model using the DevCCF P56 T2-weighted
613 template and anatomical segmentations derived from AllenCCFv3. This template-based
614 training strategy enables the model to produce accurate, multi-region parcellations without
615 requiring large-scale annotated subject data.

616 To normalize intensity across specimens, input images were preprocessed using rank-based
617 intensity normalization (`ants.rank_intensity(...)`). Spatial harmonization was achieved
618 through affine and deformable alignment of each extracted brain to the P56 template prior
619 to inference. In addition to the normalized image input, the network also receives prior
620 probability maps derived from the atlas segmentations, providing additional spatial context.
621 This general parcellation deep learning framework has also been applied in collaboration
622 with other groups pursuing related but distinct projects. In one case, a model variant was
623 adapted for T2-weighted MRI using an alternative anatomical labeling scheme; in another,
624 a separate model was developed for serial two-photon tomography (STPT) with a different
625 parcellation set. All three models are accessible through a shared interface in ANTsXNet:
626 `antspynet.mouse_brain_parcellation(...)`. Ongoing work is further extending this ap-
627 proach to embryonic mouse brain data. These independent efforts reflect broader community
628 interest in adaptable parcellation tools and reinforce the utility of ANTsXNet as a platform
629 for reproducible, extensible deep learning workflows.

630 Evaluation and reuse

631 To assess model generalizability, both the brain extraction and parcellation networks were
632 evaluated on an independent longitudinal dataset comprising multiple imaging sessions with
633 varied acquisition parameters⁷⁰. Although each label or imaging modality required re-
634 training, the process was streamlined by the reusable ANTsX infrastructure enabled by
635 rapid adaptation with minimal overhead. These results illustrate the practical benefits of a
636 template-based, low-shot strategy and modular deep learning framework. All trained mod-
637 els, associated training scripts, and supporting resources are openly available and designed
638 for straightforward integration into ANTsX workflows.

639 **Data availability**

640 All data and software used in this work are publicly available. The DevCCF atlas is
641 available at <https://kimlab.io/brain-map/DevCCF/>. ANTsPy, ANTsR, ANTsPyNet, and
642 ANTsRNet are available through GitHub at the ANTsX Ecosystem ([https://github.com/](https://github.com/ANTsX)
643 [ANTsX](#)). Training scripts for all deep learning functionality in ANTsXNet can also be
644 found on GitHub (<https://github.com/ntustison/ANTsXNetTraining>). A GitHub reposi-
645 tory specifically pertaining to the AllenCCFv3 mapping is available at <https://github.com/>
646 [dontminchenit/CCFAAlignmentToolkit](#). For the other two contributions contained in this
647 work, the longitudinal DevCCF mapping and mouse cortical thickness pipeline, we refer the
648 interested reader to <https://github.com/ntustison/ANTsXMouseBrainMapping>.

649 **Acknowledgments**

650 NIH RF1MH124605

651 Support for the research reported in this work includes funding from the National Institute
652 of Biomedical Imaging and Bioengineering (R01-EB031722) and National Institute of Mental
653 Health (RF1-MH124605, U24-MH114827, and NIH RF1MH124605 to Y.K.).

654 We also acknowledge the data contribution of Dr. Adam Raikes (GitHub @araikes) of the
655 Center for Innovation in Brain Science at the University of Arizona for refining the weights
656 of the mouse brain extraction network.

⁶⁵⁷ **Author contributions**

⁶⁵⁸ N.T., M.C., and J.G. wrote the main manuscript text and figures. M.C., M.K., R.D., S.S.,
⁶⁵⁹ Q.W., L.G., J.D., C.G., and J.G. developed the Allen registration pipelines. N.T., F.K.,
⁶⁶⁰ and Y.K. developed the time-varying velocity transformation model for the DevCCF. N.T.
⁶⁶¹ and M.T. developed the brain parcellation and cortical thickness methodology. All authors
⁶⁶² reviewed the manuscript.

663 **References**

- 664 1. Keller, P. J. & Ahrens, M. B. Visualizing whole-brain activity and development at
the single-cell level using light-sheet microscopy. *Neuron* **85**, 462–83 (2015).
- 665 2. La Manno, G. *et al.* Molecular architecture of the developing mouse brain. *Nature*
596, 92–96 (2021).
- 666 3. Wen, L. *et al.* Single-cell technologies: From research to application. *Innovation
(Camb)* **3**, 100342 (2022).
- 667 4. Oh, S. W. *et al.* A mesoscale connectome of the mouse brain. *Nature* **508**, 207–14
(2014).
- 668 5. Gong, H. *et al.* Continuously tracing brain-wide long-distance axonal projections in
mice at a one-micron voxel resolution. *Neuroimage* **74**, 87–98 (2013).
- 669 6. Li, A. *et al.* Micro-optical sectioning tomography to obtain a high-resolution atlas of
the mouse brain. *Science* **330**, 1404–8 (2010).
- 670 7. Ueda, H. R. *et al.* Tissue clearing and its applications in neuroscience. *Nat Rev
Neurosci* **21**, 61–79 (2020).
- 671 8. Ståhl, P. L. *et al.* Visualization and analysis of gene expression in tissue sections by
spatial transcriptomics. *Science* **353**, 78–82 (2016).
- 672 9. Burgess, D. J. Spatial transcriptomics coming of age. *Nat Rev Genet* **20**, 317 (2019).
- 673 10. Hardwick, S. A. *et al.* Single-nuclei isoform RNA sequencing unlocks barcoded exon
connectivity in frozen brain tissue. *Nature biotechnology* **40**, 1082–1092 (2022).
- 674 11. Hawrylycz, M. *et al.* A guide to the BRAIN initiative cell census network data
ecosystem. *PLoS biology* **21**, e3002133 (2023).
- 675 12. Wang, Q. *et al.* The allen mouse brain common coordinate framework: A 3D reference
atlas. *Cell* **181**, 936–953.e20 (2020).
- 676 13. Perens, J. *et al.* An optimized mouse brain atlas for automated mapping and quantification
of neuronal activity using iDISCO+ and light sheet fluorescence microscopy.
Neuroinformatics **19**, 433–446 (2021).
- 677 14. Ma, Y. *et al.* A three-dimensional digital atlas database of the adult C57BL/6J mouse
brain by magnetic resonance microscopy. *Neuroscience* **135**, 1203–1215 (2005).

- 678 15. Qu, L. *et al.* Cross-modal coherent registration of whole mouse brains. *Nature Methods* **19**, 111–118 (2022).
- 679 16. Kronman, F. N. *et al.* [Developmental mouse brain common coordinate framework](#). *Nat Commun* **15**, 9072 (2024).
- 680 17. Chuang, N. *et al.* An MRI-based atlas and database of the developing mouse brain. *Neuroimage* **54**, 80–89 (2011).
- 681 18. Dries, R. *et al.* Advances in spatial transcriptomic data analysis. *Genome research* **31**, 1706–1718 (2021).
- 682 19. Ricci, P. *et al.* Removing striping artifacts in light-sheet fluorescence microscopy: A review. *Progress in biophysics and molecular biology* **168**, 52–65 (2022).
- 683 20. Agarwal, N., Xu, X. & Gopi, M. Robust registration of mouse brain slices with severe histological artifacts. in *Proceedings of the tenth indian conference on computer vision, graphics and image processing* 1–8 (2016).
- 684 21. Agarwal, N., Xu, X. & Gopi, M. Automatic detection of histological artifacts in mouse brain slice images. in *Medical computer vision and bayesian and graphical models for biomedical imaging: MICCAI 2016 international workshops, MCV and BAMBI, athens, greece, october 21, 2016, revised selected papers* 8 105–115 (Springer, 2017).
- 685 22. Tward, D. *et al.* 3d mapping of serial histology sections with anomalies using a novel robust deformable registration algorithm. in *International workshop on multimodal brain image analysis* 162–173 (Springer, 2019).
- 686 23. Cahill, L. S. *et al.* Preparation of fixed mouse brains for MRI. *Neuroimage* **60**, 933–939 (2012).
- 687 24. Biancalani, T. *et al.* [Deep learning and alignment of spatially resolved single-cell transcriptomes with tangram](#). *Nat Methods* **18**, 1352–1362 (2021).
- 688 25. Sunkin, S. M. *et al.* Allen brain atlas: An integrated spatio-temporal portal for exploring the central nervous system. *Nucleic acids research* **41**, D996–D1008 (2012).
- 689 26. Kim, Y. *et al.* Brain-wide maps reveal stereotyped cell-type-based cortical architecture and subcortical sexual dimorphism. *Cell* **171**, 456–469 (2017).

- 690 27. Fürth, D. *et al.* An interactive framework for whole-brain maps at cellular resolution. *Nat Neurosci* **21**, 139–149 (2018).
- 691 28. Li, Y. *et al.* mBrainAligner-web: A web server for cross-modal coherent registration of whole mouse brains. *Bioinformatics* **38**, 4654–4655 (2022).
- 692 29. Puchades, M. A., Csucs, G., Ledergerber, D., Leergaard, T. B. & Bjaalie, J. G. Spatial registration of serial microscopic brain images to three-dimensional reference atlases with the QuickNII tool. *PloS one* **14**, e0216796 (2019).
- 693 30. Eastwood, B. S. *et al.* Whole mouse brain reconstruction and registration to a reference atlas with standard histochemical processing of coronal sections. *Journal of Comparative Neurology* **527**, 2170–2178 (2019).
- 694 31. Ni, H. *et al.* A robust image registration interface for large volume brain atlas. *Sci Rep* **10**, 2139 (2020).
- 695 32. Pallast, N. *et al.* Processing pipeline for atlas-based imaging data analysis of structural and functional mouse brain MRI (AIDAmri). *Front Neuroinform* **13**, 42 (2019).
- 696 33. Celestine, M., Nadkarni, N. A., Garin, C. M., Bougacha, S. & Dhenain, M. Sammba-MRI: A library for processing SmAll-MaMmal BrAin MRI data in python. *Front Neuroinform* **14**, 24 (2020).
- 697 34. Ioanas, H.-I., Marks, M., Zerbi, V., Yanik, M. F. & Rudin, M. An optimized registration workflow and standard geometric space for small animal brain imaging. *Neuroimage* **241**, 118386 (2021).
- 698 35. Aggarwal, M., Zhang, J., Miller, M. I., Sidman, R. L. & Mori, S. Magnetic resonance imaging and micro-computed tomography combined atlas of developing and adult mouse brains for stereotaxic surgery. *Neuroscience* **162**, 1339–1350 (2009).
- 699 36. Chandrashekhar, V. *et al.* CloudReg: Automatic terabyte-scale cross-modal brain volume registration. *Nature methods* **18**, 845–846 (2021).
- 700 37. Jin, M. *et al.* SMART: An open-source extension of WholeBrain for intact mouse brain registration and segmentation. *eNeuro* **9**, (2022).
- 701 38. Negwer, M. *et al.* FriendlyClearMap: An optimized toolkit for mouse brain mapping and analysis. *Gigascience* **12**, (2022).

- 702 39. Lin, W. *et al.* Whole-brain mapping of histaminergic projections in mouse brain. *Proceedings of the National Academy of Sciences* **120**, e2216231120 (2023).
- 703 40. Zhang, M. *et al.* Spatially resolved cell atlas of the mouse primary motor cortex by MERFISH. *Nature* **598**, 137–143 (2021).
- 704 41. Shi, H. *et al.* Spatial atlas of the mouse central nervous system at molecular resolution. *Nature* **622**, 552–561 (2023).
- 705 42. Zhang, Y. *et al.* Reference-based cell type matching of *in situ* image-based spatial transcriptomics data on primary visual cortex of mouse brain. *Scientific Reports* **13**, 9567 (2023).
- 706 43. Klein, S., Staring, M., Murphy, K., Viergever, M. A. & Pluim, J. P. W. [Elastix: A toolbox for intensity-based medical image registration](#). *IEEE Trans Med Imaging* **29**, 196–205 (2010).
- 707 44. Fedorov, A. *et al.* 3D slicer as an image computing platform for the quantitative imaging network. *Magnetic resonance imaging* **30**, 1323–1341 (2012).
- 708 45. Tustison, N. J. *et al.* [The ANTsX ecosystem for quantitative biological and medical imaging](#). *Sci Rep* **11**, 9068 (2021).
- 709 46. Pagani, M., Damiano, M., Galbusera, A., Tsafaris, S. A. & Gozzi, A. Semi-automated registration-based anatomical labelling, voxel based morphometry and cortical thickness mapping of the mouse brain. *Journal of neuroscience methods* **267**, 62–73 (2016).
- 710 47. Anderson, R. J. *et al.* [Small animal multivariate brain analysis \(SAMBA\) - a high throughput pipeline with a validation framework](#). *Neuroinformatics* **17**, 451–472 (2019).
- 711 48. Allan Johnson, G. *et al.* Whole mouse brain connectomics. *Journal of Comparative Neurology* **527**, 2146–2157 (2019).
- 712 49. Yao, Z. *et al.* [A high-resolution transcriptomic and spatial atlas of cell types in the whole mouse brain](#). *Nature* **624**, 317–332 (2023).
- 713 50. Avants, B. B., Epstein, C. L., Grossman, M. & Gee, J. C. [Symmetric diffeomorphic image registration with cross-correlation: Evaluating automated labeling of elderly and neurodegenerative brain](#). *Med Image Anal* **12**, 26–41 (2008).

- 714 51. Tustison, N. J. *et al.* N4ITK: Improved N3 bias correction. *IEEE Trans Med Imaging* **29**, 1310–20 (2010).
- 715 52. Bajcsy, R. & Broit, C. Matching of deformed images. in *Sixth International Conference on Pattern Recognition (ICPR'82)* 351–353 (1982).
- 716 53. Bajcsy, R. & Kovacic, S. Multiresolution elastic matching. *Computer Vision, Graphics, and Image Processing* **46**, 1–21 (1989).
- 717 54. Gee, J. C., Reivich, M. & Bajcsy, R. Elastically deforming 3D atlas to match anatomical brain images. *J Comput Assist Tomogr* **17**, 225–36 (1993).
- 718 55. Klein, A. *et al.* Evaluation of 14 nonlinear deformation algorithms applied to human brain MRI registration. *Neuroimage* **46**, 786–802 (2009).
- 719 56. Murphy, K. *et al.* Evaluation of registration methods on thoracic CT: The EMPIRE10 challenge. *IEEE Trans Med Imaging* **30**, 1901–20 (2011).
- 720 57. Baheti, B. *et al.* The brain tumor sequence registration challenge: Establishing correspondence between pre-operative and follow-up MRI scans of diffuse glioma patients. (2021).
- 721 58. Roston, R. A., Tustison, N. J. & Maga, A. M. Anatomy-aware, label-informed approach improves image registration for challenging datasets. *bioRxiv* (2025) doi:10.1101/2025.08.11.669599.
- 722 59. Avants, B. B. *et al.* The optimal template effect in hippocampus studies of diseased populations. *Neuroimage* **49**, 2457–66 (2010).
- 723 60. Avants, B. B., Tustison, N. J., Wu, J., Cook, P. A. & Gee, J. C. An open source multivariate framework for n-tissue segmentation with evaluation on public data. *Neuroinformatics* **9**, 381–400 (2011).
- 724 61. Manjón, J. V., Coupé, P., Martí-Bonmatí, L., Collins, D. L. & Robles, M. Adaptive non-local means denoising of MR images with spatially varying noise levels. *J Magn Reson Imaging* **31**, 192–203 (2010).
- 725 62. Wang, H. *et al.* Multi-atlas segmentation with joint label fusion. *IEEE Trans Pattern Anal Mach Intell* **35**, 611–23 (2013).

- 726 63. Tustison, N. J. *et al.* Optimal symmetric multimodal templates and concatenated random forests for supervised brain tumor segmentation (simplified) with *ANTsR*. *Neuroinformatics* (2014) doi:[10.1007/s12021-014-9245-2](https://doi.org/10.1007/s12021-014-9245-2).
- 727 64. Tustison, N. J., Yang, Y. & Salerno, M. **Advanced normalization tools for cardiac motion correction**. in *Statistical atlases and computational models of the heart - imaging and modelling challenges* (eds. Camara, O. et al.) vol. 8896 3–12 (Springer International Publishing, 2015).
- 728 65. McCormick, M., Liu, X., Jomier, J., Marion, C. & Ibanez, L. **ITK: Enabling reproducible research and open science**. *Front Neuroinform* **8**, 13 (2014).
- 729 66. Beg, M. F., Miller, M. I., Trouvé, A. & Younes, L. **Computing large deformation metric mappings via geodesic flows of diffeomorphisms**. *International Journal of Computer Vision* **61**, 139–157 (2005).
- 730 67. Tustison, N. J. & Avants, B. B. **Explicit B-spline regularization in diffeomorphic image registration**. *Front Neuroinform* **7**, 39 (2013).
- 731 68. Hsu, L.-M. *et al.* CAMRI mouse brain MRI data.
- 732 69. Reshetnikov, V. *et al.* High-resolution MRI data of brain C57BL/6 and BTBR mice in three different anatomical views.
- 733 70. Rahman, N., Xu, K., Budde, M. D., Brown, A. & Baron, C. A. **A longitudinal microstructural MRI dataset in healthy C57Bl/6 mice at 9.4 tesla**. *Sci Data* **10**, 94 (2023).
- 734 71. Liu, J. *et al.* **Concordance of MERFISH spatial transcriptomics with bulk and single-cell RNA sequencing**. *Life Sci Alliance* **6**, (2023).
- 735 72. Stringer, C., Wang, T., Michaelos, M. & Pachitariu, M. **Cellpose: A generalist algorithm for cellular segmentation**. *Nat Methods* **18**, 100–106 (2021).
- 736 73. Jia, H., Yap, P.-T., Wu, G., Wang, Q. & Shen, D. **Intermediate templates guided groupwise registration of diffusion tensor images**. *NeuroImage* **54**, 928–939 (2011).
- 737 74. Tang, S., Fan, Y., Wu, G., Kim, M. & Shen, D. **RABBIT: Rapid alignment of brains by building intermediate templates**. *NeuroImage* **47**, 1277–1287 (2009).

- 738 75. Dewey, B. E., Carass, A., Blitz, A. M. & Prince, J. L. Efficient multi-atlas registration using an intermediate template image. in *Proceedings of SPIE—the international society for optical engineering* vol. 10137 (NIH Public Access, 2017).
- 739 76. Perens, J. *et al.* Multimodal 3D mouse brain atlas framework with the skull-derived coordinate system. *Neuroinformatics* **21**, 269–286 (2023).
- 740 77. Rotolo, T., Smallwood, P. M., Williams, J. & Nathans, J. Genetically-directed, cell type-specific sparse labeling for the analysis of neuronal morphology. *PLoS One* **3**, e4099 (2008).
- 741 78. Peng, H. *et al.* Morphological diversity of single neurons in molecularly defined cell types. *Nature* **598**, 174–181 (2021).
- 742 79. Gong, H. *et al.* High-throughput dual-colour precision imaging for brain-wide connectome with cytoarchitectonic landmarks at the cellular level. *Nat Commun* **7**, 12142 (2016).
- 743 80. Wang, J. *et al.* Divergent projection patterns revealed by reconstruction of individual neurons in orbitofrontal cortex. *Neurosci Bull* **37**, 461–477 (2021).
- 744 81. Avants, B. B. *et al.* The Insight ToolKit image registration framework. *Front Neuroinform* **8**, 44 (2014).
- 745 82. Chon, U., Vanselow, D. J., Cheng, K. C. & Kim, Y. Enhanced and unified anatomical labeling for a common mouse brain atlas. *Nat Commun* **10**, 5067 (2019).
- 746 83. Tasic, B. *et al.* Adult mouse cortical cell taxonomy revealed by single cell transcriptomics. *Nat Neurosci* **19**, 335–46 (2016).
- 747 84. Bergmann, E., Gofman, X., Kavushansky, A. & Kahn, I. Individual variability in functional connectivity architecture of the mouse brain. *Commun Biol* **3**, 738 (2020).
- 748 85. Billot, B. *et al.* SynthSeg: Segmentation of brain MRI scans of any contrast and resolution without retraining. *Med Image Anal* **86**, 102789 (2023).
- 749 86. Rolfe, S. M., Whikehart, S. M. & Maga, A. M. Deep learning enabled multi-organ segmentation of mouse embryos. *Biol Open* **12**, bio059698 (2023).

- 750 87. Tustison, N. J. & Gee, J. C. Generalized n -d C^k B-spline scattered data approximation
with confidence values. in *Medical imaging and augmented reality* (eds. Yang, G.-Z.,
Jiang, T., Shen, D., Gu, L. & Yang, J.) 76–83 (Springer Berlin Heidelberg, 2006).
- 751 88. Falk, T. *et al.* U-net: Deep learning for cell counting, detection, and morphometry.
Nat Methods **16**, 67–70 (2019).
- 752 89. Isensee, F., Jaeger, P. F., Kohl, S. A. A., Petersen, J. & Maier-Hein, K. H. nnU-net:
A self-configuring method for deep learning-based biomedical image segmentation.
Nat Methods **18**, 203–211 (2021).
- 753 90. Tustison, N. J. *et al.* Image- versus histogram-based considerations in semantic seg-
mentation of pulmonary hyperpolarized gas images. *Magn Reson Med* **86**, 2822–2836
(2021).